ITC 3/55
Information Technology and Control
Vol. 55 / No. 3/ 2026
pp. 1365-1382
DOI 10.5755/j01.itc.55.3.43931

ANN-APFFT Harmonic Detection Method Considering Power System Security

Received 2025/12/25 | Accepted after revision 2026/05/22

HOW TO CITE: Zhang, L., Wang, X. (2026) ANN-APFFT Harmonic Detection Method Considering Power System Security. *Information Technology and Control*, 55(3), 1364-1381. https://doi.org/10.5755/j01.itc.55.3.43931

ANN-APFFT Harmonic Detection Method Considering Power System Security

Li Zhang*
College of Computer and Information Engineering; Inner Mongolia Agricultural University; Hohhot, 010010, China; e-mail: LiZhangaz@outlook.com

Xiaoyu Wang
State Grid Inner Mongolia East Electric Power Co., Ltd; Power Dispatching and Control Center; Hohhot, 010010, China; e-mail: wangxiaoyu1005@163.com

Corresponding author: LiZhangaz@outlook.com

This study proposes a harmonic detection method based on artificial neural network and all-phase Fast Fourier Transform to solve three problems in power systems: inaccurate nonlinear feature extraction, noise sensitivity, and slow dynamic response. It uses adaptive particle swarm optimization algorithm to improve neural network parameter initialization and sparse decomposition to enhance spectrum anti_interference ability. This builds a tandem architecture for rapid feature extraction and precise parameter estimation. Experimental results revealed that the phase measurement accuracy reached 2.05°, and under standard simulation conditions the frequency tracking error did not exceed 40mHz. The average signal-to-noise ratio improvement reached 12.3dB across the tested noisy environments. Meanwhile, the algorithm convergence time of this method in transient events such as motor starting, capacitor switching, and short-circuit faults was reduced to within 105ms, 50ms, and 150ms, respectively. The research integrates intelligent feature learning with precision spectrum analysis. It effectively balances accuracy and robustness in harmonic detection for complex power grids. This provides technical support for power quality monitoring and safety assessment.

KEYWORDS: Harmonic Detection, Artificial Neural Network, All-Phase Fast Fourier Transform, Adaptive Particle Swarm Optimization, Sparse Decomposition, Power Security

1. Background

Accurate perception and security assessment of power system operating status are important tasks in smart grid. In complex power supply environments, power harmonics and interharmonic signals form a nonlinear dataset that has key diagnostic value but is difficult to analyze [2]. These signals are non_stationary, non_linear, and noise_prone. They contain complex components (fundamental, harmonics, interharmonics), dynamic characteristics (amplitude/phase fluctuation, frequency offset), and mixed Gaussian/non_Gaussian noise. Traditional harmonic analysis based on fast Fourier transform (FFT) and its improved algorithms has significant limitations in spectrum leakage, noise suppression, and unbiased phase measurement [25]. Therefore, developing a robust harmonic detection framework with high_precision parameter estimation is a key challenge for safe and stable power system operation. Many researchers have studied this topic.

Wang et al. [24] proposed a general probabilistic modeling method based on operating state identification. This method solves the problem of low accuracy caused by uncertain operating states in power system harmonic modeling. It improves the modeling accuracy of harmonic emission characteristics and enhances model generalization by identifying load operating states and constructing probability density functions [24]. Zhang et al. [26] established a harmonic detection optimization method based on a small signal model. This method addresses the harmonic oscillation problem caused by the full compensation mode of a shunt active power filter. It constructs a correlation model between system impedance and harmonic transfer characteristics to accurately identify the oscillation mechanism. It also improves harmonic detection accuracy and adaptability under complex grid conditions [26]. Song et al. [20] proposed a passive islanding detection method based on harmonic coupling characteristics. This method solves the problem of islanding detection failure caused by harmonic interference in high-penetration grid-connected inverters. It analyzes harmonic spectrum characteristics and disturbance propagation rules under multi-inverter interaction. It can accurately identify the islanding state in complex harmonic environments and maintain detection reliability [20]. Liu et al. [12] proposed a joint detection algorithm based on singular value decomposition and Hilbert transform. This algorithm solves the problem of accurate harmonic parameter detection under compound disturbances in ship power grids. It uses singular value decomposition for noise reduction and Hilbert spectrum analysis. It can accurately identify the amplitude and frequency of each harmonic and maintain high computational efficiency in various complex interference environments [12].

In addition, Wang et al. [23] proposed the two-step improved ensemble empirical mode decomposition-based harmonic detection method (TIEEMD) to solve fundamental wave attenuation and mode aliasing in active power filter harmonic detection. This method combines parameterized white noise and analytical signal injection with a noise-dominant component reconstruction strategy. It effectively suppresses modal mixing, reduces fundamental wave energy attenuation, and improves the model's adaptability to non-stationary harmonic signals [23]. Fei et al. [5] proposed the wavelet fuzzy neural network and super-twisting sliding mode-based hybrid detection method (WFN-STS). This method addresses the difficulty of balancing real-time performance and accuracy in active power filter harmonic detection. It enhances feature extraction through the wavelet layer and uses Lyapunov stability theory to design adaptive parameter laws. It achieves rapid and accurate harmonic detection and control under nonlinear load conditions [5]. Rodrigues et al. [16] proposed the real-grid signal database-based deep learning detection method (RSDDL). This method overcomes the limitations of traditional power quality event detection methods that rely on analog signals. It trains deep neural networks using actual signals collected by grid monitoring equipment. It effectively improves the detection accuracy and engineering applicability for power quality events such as harmonics [16]. Kuyumani et al. [10] proposed a harmonic detection method that integrates convolutional neural network (CNN) and long short-term memory network (LSTM). This method solves the problem of low detection accuracy caused by the nonlinear and non-stationary characteristics of smart grid harmonics. It uses CNN

to extract spatial features and LSTM to capture time dependence. This synergy enables precise extraction of spatiotemporal features from harmonic signals and improves prediction accuracy [10].

To sum up, existing research achieves harmonic feature extraction, adaptability to nonlinear signals, and improved detection robustness. However, existing methods still have core problems. These include a lack of closed-loop feedback and information interaction between feature extraction and parameter estimation modules. They are also sensitive to noise and interharmonic interference. In addition, there is an imbalance between model accuracy and efficiency.

Artificial neural network (ANN) has powerful feature adaptive learning and pattern recognition capabilities. It does this through nonlinear mapping of multi-layer neurons [18]. All-phase FFT (APFFT) can effectively suppress spectral leakage and provide unbiased phase measurement. It uses a unique dual-window convolution and cyclic shift structure [11]. However, the convergence and solution quality of ANN heavily depend on the initial parameters.

Table 1

Comparison between the proposed method and state-of-the-art methods.

Method	Advantages	Key findings	References
ANN-only	Adaptive nonlinear mapping to extract harmonic features from complex signals	Using ANN alone struggles to balance amplitude, phase, and frequency detection accuracy, especially in noisy environments	/
APSO-ANN	APSO globally optimises initial ANN weights/thresholds, improving convergence speed and prediction accuracy	APSO improves initial parameter quality of ANN but cannot solve spectral leakage or phase deviation problems	/
APFFT	Phase invariance, calibration-free high-precision phase measurement; suppresses spectral leakage	APFFT has clear advantages in phase measurement under clean conditions, but noise immunity is its bottleneck	/
SDS-APFFT	SDS pre_processing improves input spectral purity for APFFT, enhancing noise robustness	Sparse filtering effectively suppresses noise, but without front_end feature guidance, it still risks incorrect atom selection in complex harmonic scenarios	/
TIEEMD	Two_step improved ensemble empirical mode decomposition, mitigates mode mixing	Signal decomposition methods have some adaptability to non_stationary harmonics, but endpoint effects and mode mixing limit phase measurement accuracy	[23]
WFN-STS	Combines wavelet fuzzy neural network with super_twisting sliding mode for fast detection and control	Combining intelligent control with neural networks enables fast detection, but response to phase changes is insufficient	[5]
RSDDL	Deep network trained on real_grid data, good engineering applicability	Deep learning methods rely on data quality; phase labelling errors in real grids propagate to detection results	[10]
CNLS	Joint spatiotemporal feature extraction, suitable for harmonic prediction and detection	CNN_LSTM effectively extracts spatiotemporal features, but long_sequence modelling bias affects frequency tracking accuracy	[18]
A-AHDM	1) APSO_ANN intelligent pre_extraction; 2) SDS_APFFT precise estimation; 3) frequency_band mask constraint; 4) closed_loop feedback correction. Best accuracy_robustness_efficiency trade_off	Through dual_module series architecture and closed_loop feedback, it achieves synergy between intelligent feature learning and precise mathematical analysis, significantly improving detection accuracy and robustness in complex noise environments while maintaining computational efficiency	Ours

ANN is also prone to falling into local optima. The analysis accuracy and robustness of APFFT significantly decrease in strong noise or complex spectrum environments [8, 21].

Therefore, this research is based on the basic logic of ANN and APFFT. It introduces adaptive particle swarm optimization (APSO) and sparse decomposition strategy (SDS). Finally, it proposes the ANN-APFFT-based harmonic detection model (A-AHDM). The research aims to build a safety-oriented harmonic detection framework. This framework integrates intelligent feature extraction and mathematical precision analysis. It solves the dual limitations of traditional methods in robustness and accuracy. The comparison between the proposed method and state-of-the-art methods is shown in Table 1.

The technical novelty of this research lies in constructing a dual-module series architecture of APSO-ANN and SDS-APFFT, introducing a frequency-band mask constraint that uses the key frequency bands identified by the front-end as the limited search region for back-end sparse decomposition, and simultaneously designing a closed-loop feedback correction mechanism that leverages the high-precision results from the back-end to inversely correct the front-end output. This achieves deep synergy between intelligent feature learning and precise mathematical analysis, rather than a simple modular stacking of known components.

2. Methods and Materials

This part consists of two core sections. The first section uses ANN as the core framework and combines with the APSO optimization algorithm to build an adaptive extraction and preliminary identification module of harmonic features. The second section establishes a high-precision parameter estimation module integrating APFFT and SDS, and finally integrates the ANN-APFFT-based harmonic detection model (A-AHDM). The series-connected dual modules form a collaborative mechanism of rapid feature extraction and precise parameter estimation, which effectively improves the accuracy and robustness of harmonic detection in power systems.

2.1. Preliminary Extraction of Harmonic Features Based on ANN

The modern power system integrates power generation, transmission, distribution, and consumption. Its safe operation is crucial for society and the economy. Nonlinear loads cause serious harmonic pollution, leading to equipment overheating, protection malfunction, and insulation aging, which threaten system reliability. Thus, accurate harmonic detection and feature identification are key to ensuring power quality and system safety. ANN has powerful nonlinear mapping and adaptive learning. It extracts

Figure 1
Schematic diagram of ANN structure.

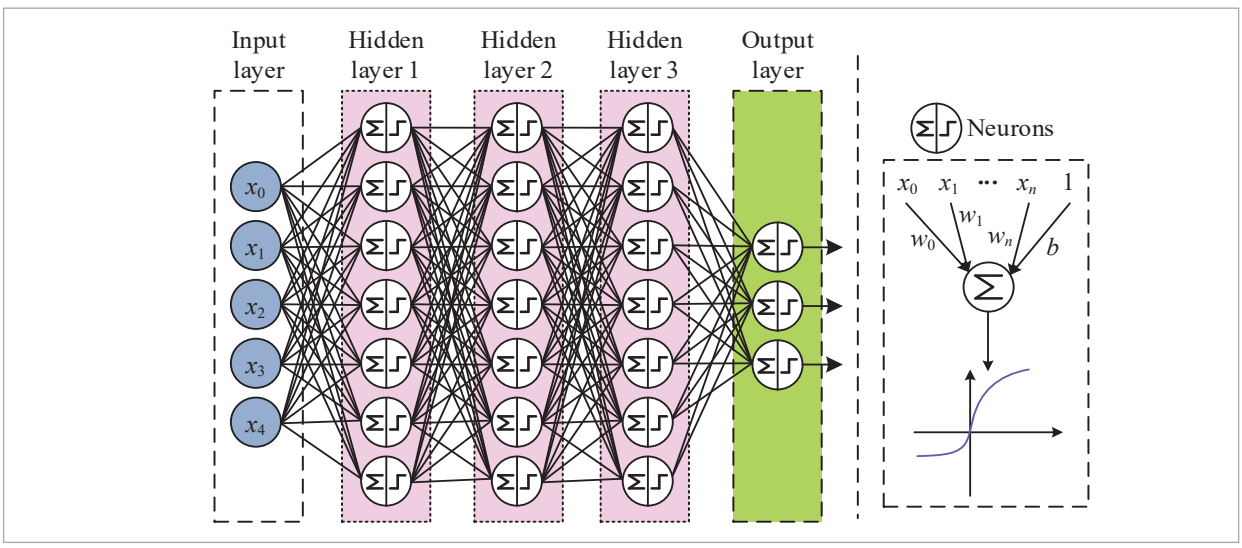
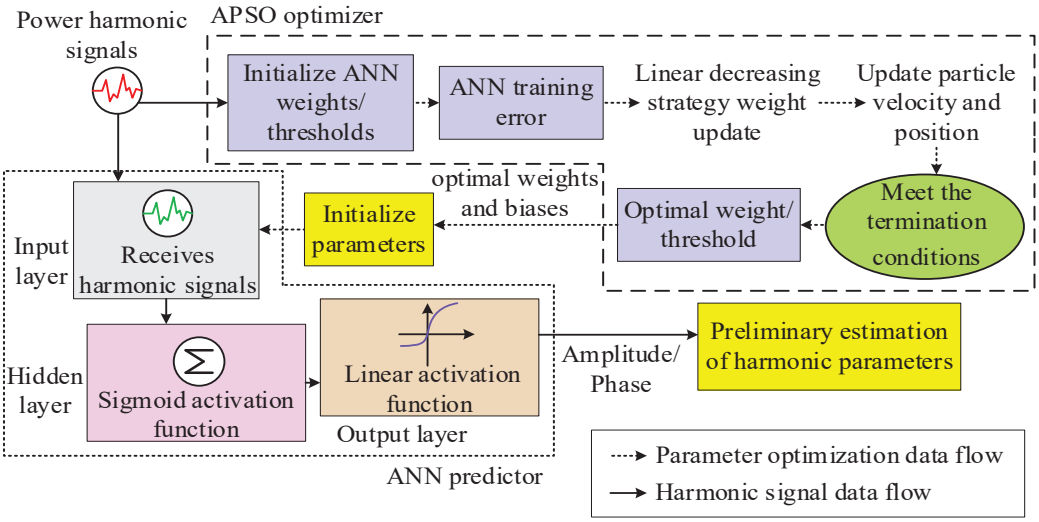


Figure 2

Schematic diagram of the structure of the harmonic feature preliminary extraction module.



hidden features from complex electrical signals and suits non-stationary, multi-frequency harmonic analysis [1]. Thus, this study uses ANN to build an adaptive harmonic feature extraction and preliminary identification model, as shown in Figure 1.

In Figure 1, the model adopts a typical three-layer feedforward neural network architecture, including an input layer, a single hidden layer, and an output layer. The harmonic signal is input into the network after preprocessing. The preprocessing uses a sampling frequency of 12.8 kHz (256 points per cycle), segments the signal with a Hanning window over 10–50 cycles, normalises the amplitude by the maximum absolute value to [-1,1], applies an anti-aliasing low-pass filter with a cut-off frequency of 6.4 kHz, and achieves a frequency resolution of 0.2 Hz. Moreover, through the weighted operation and nonlinear transformation of the hidden layer, the preliminary estimation result of the harmonic parameters is finally generated by the output layer [22]. First, the preprocessed harmonic signals are sampled to construct a training data set. It is assumed that the input vector is $\mathbf{X}=[x_1,x_2,\ldots,x_n]^T$, corresponding to the expected output vector $\mathbf{Y}=[y_1,y_2,\ldots,y_m]^T$. Among them, n is the number of input nodes and m is the number of output nodes. In the hidden layer, the net input net_j of the j-th neuron and its activation output h_j are shown in Equation (1) [17].

$$\begin{cases} \text{net}_j = \sum_{i=1}^{n} w_{ji} x_i + b_j \\ h_j = f(\text{net}_j) \end{cases}. \tag{1}$$

In Equation (1), w_{ji} is the connection weight from the input layer to the hidden layer. b_j is the corresponding bias term. $f(\cdot)$ uses a Sigmoid activation function, that is, $f(z)=1/1+e^{-z}$. In the output layer, the output of the k-th neuron is o_k, as shown in Equation (2).

$$o_k = g\left(\sum_{j=1}^{L} w_{kj} h_j + b_k\right). \tag{2}$$

In Equation (2), L is the number of neurons in the hidden layer. w_{kj} is the weight from the hidden layer to the output layer. b_k is the output layer bias. $g(\cdot)$ uses a linear activation function to adapt to continuous value output requirements. Moreover, the research defines the loss function of ANN as mean square error (MSE), as shown in Equation (3).

$$E = \frac{1}{2}\sum_{k=1}^{m}(y_k - o_k)^2. \tag{3}$$

In Equation (3), E is the loss function value. The ANNs are configured with the number of input nodes

equal to the number of sampling points (e.g., 256 × number of cycles), 32 nodes in the hidden layer, and the number of output nodes equal to the harmonic order × 2 (amplitude and frequency position). The learning rate is 0.001, the Adam optimizer is used, the batch size is 64, the number of training epochs is 200, early stopping is applied (validation loss does not decrease for 10 consecutive epochs), and Xavier uniform initialisation is adopted. The stopping criterion is that the loss does not decrease for 10 consecutive epochs [9]. Training stops when the loss function converges or the preset epoch is reached. However, ANN easily falls into local optima, and its convergence speed and solution quality depend heavily on initial parameters. APSO has strong global search and adaptively avoids premature convergence. Thus, we use APSO to optimize ANN's initial weights and thresholds, improving convergence speed and accuracy. APSO explores the parameter space via swarm collaboration and adaptive inertia weights, avoiding local minima in the ANN loss function and providing a better starting point for gradient descent [13]. Moreover, APSO uses adaptive inertia weight and group guidance. Particles explore widely in early iterations and search locally later. This avoids local minima in the ANN loss function and gives a better initial point for gradient descent [14]. The details are as follows: first, all the parameters to be optimized (weights and thresholds) of the ANN are encoded into an D-dimensional vector, which constitutes the position $\mathbf{X}_i=[x_{i1},x_{i2},...,x_{iD}]$ of a particle. Each particle i also has a speed $\mathbf{V}_i=[v_{i1},v_{i2},...,v_{iD}]$. In each iteration of each generation, each particle dynamically adjusts its flight direction according to its own historical optimal solution (individual extreme value) and the group's global optimal solution (global extreme value). Let the individual optimal position of the i-th particle in the k-th generation be $\mathbf{P}_i^k$, and the group optimal position be $\mathbf{P}_g^k$. Its speed and position updates are shown in Equation (4) [4].

$$\begin{cases} v_{id}^{k+1} = \omega v_{id}^{k} + c_1 r_1 (p_{id}^{k} - x_{id}^{k}) + c_2 r_2 (p_{gd}^{k} - x_{id}^{k}) \\ x_{id}^{k+1} = x_{id}^{k} + v_{id}^{k+1} \end{cases}. \quad (4)$$

In Equation (4), ω is the inertia weight, which is used to balance global exploration and local development capabilities. $\{c_1,c_2\}$ is the learning factor, with an experience value of 2.0, used to control the influence of individual and group experience [6]. $\{r_1,r_2\}$ is a uniformly distributed random number in the interval [0, 1], which is used to introduce search randomness. In order to improve the search efficiency, a linearly decreasing adaptive inertia weight strategy is studied, as shown in Equation (5).

$$\omega = \omega_{\max} - \frac{k}{K_{\max}}(\omega_{\max} - \omega_{\min}). \quad (5)$$

In Equation (5), $\{\omega_{\max},\omega_{\min}\}$ is the initial and terminal inertia weight (grid search 0.9→0.4). k is the current iteration number. $K_{\max}$ is the maximum number of iterations. This strategy maintains a large ω in the early iteration to enhance global exploration capabilities, and reduces ω in the later stage to enhance local fine search and prevent oscillation [7]. Finally, the parameter set represented by $\mathbf{P}_g$ will be assigned to the ANN for subsequent training. APSO has a swarm size of 30, maximum 100 iterations, velocity bounds [-0.5,0.5], position bounds determined by weight/threshold range (e.g., [-5,5]), fitness function is validation MSE, stopping criterion is completing iterations or global best unchanged for 20 generations. APSO optimises all weights and biases (all trainable parameters) of the ANN. Therefore, the APSO algorithm is studied as the pre-optimizer of ANN and a preliminary harmonic feature extraction module based on ANN-APSO is established. Its structure is shown in Figure 2.

In Figure 2, this module consists of APSO optimizer and ANN predictor that are connected back and forth. The preprocessed power harmonic signal data is first input into the APSO optimizer, which uses the validation set MSE of the ANN as the fitness function and searches for the best initial weight and threshold combination of the ANN through group iterative search. After the search is completed, the optimal solution obtained is used to initialize the network parameters of the ANN. APSO runs once offline before training, using the validation set MSE as the fitness function. After obtaining the optimal initial parameters, the ANN is retrained on the training set using gradient descent (the Adam optimizer). APSO does not participate in subsequent folds or online updates. After that, the signal data is officially input into the optimized ANN for forward propagation calculation. Its output layer directly generates

preliminary estimates of the amplitude and frequency position of each harmonic.

2.2. High-Precision Harmonic Parameter Estimation and A-AHDM Model Establishment Based on APFFT

The ANN-APSO module provides reliable initial results but has limited phase and frequency resolution. APFFT has phase invariance, suppresses spectrum leakage and fence effects, and improves frequency, amplitude, and phase measurements. Its outputs need no correction and suit real-time monitoring. Thus, we build a high-precision harmonic estimator using APFFT, as shown in Figure 3.

In Figure 3, the framework first constructs a full-phase data segment with a length of 2N-1 for the central sample point. After weighted preprocessing by the convolution window, it is then sent to the N-point FFT core operation, and finally directly outputs a high-precision spectrum with correction-free characteristics. Given the input discrete signal sequence $x(n)$, with the current analysis moment n_0 as the center, a symmetrical data segment with a length of $2N–1$ is intercepted, as shown in Equation (6).

$$\mathbf{x}_{ap} = [x(n_0 - N + 1),...,x(n_0),...,x(n_0 + N - 1)]. \quad (6)$$

The window shown in Equation (6) can cover $N–1$ sampling points before and after the center point, ensuring the complete capture of local signal characteristics. Afterwards, a convolution window function $w_c(m)$ of length $2N–1$ is used to weight the data segments to further suppress spectrum leakage. The convolution window is obtained by linear convolution and normalization of two basic window functions $w_a(m)$ and $w_b(m)$ of length N, as shown in Equation (7).

$$w_c(m) = \frac{(w_a * w_b)(m)}{\sum_{m=-(N-1)}^{N-1} w_c(m)},\ m = -(N-1),\ldots,0,\ldots,N-1. \quad (7)$$

Equation (7) is selected as a double Hanning window, which can effectively improve the side lobe attenuation performance. The weighted data is specially processed to achieve intrinsic phase correction by introducing a complex exponential weighting factor. A new point N input sequence $y(k)$ is constructed, as shown in Equation (8).

$$y(k) = \sum_{m=-(N-1)}^{N-1} x(n_0 + m) \cdot w_c(m) \cdot e^{-j\frac{2\pi}{N}mk},\ k = 0,1,\ldots,N-1. \quad (8)$$

Equation (8) essentially completes the fusion operation of time domain weighting and frequency domain phase pre-compensation, which is equivalent to "aligning" all phase information to the central sampling point n_0. Finally, the standard N-point FFT operation is performed on the generated N point sequence $y(k)$ to obtain the final spectrum output $Y(k)$=FFT[$y(k)$] (k=0,1,...,N–1). The phase information in this result is the true phase of the signal at time n_0, and no additional correction is required. In this study, he specific parameters of APFFT are as follows: N=1024, the full-phase segment length is 2047 points, the phase reference point is the central sampling point, frequency estimation is directly obtained by multiplying the peak spectral line position by the frequency resolution (0.2 Hz) without interpolation, and the window function is fixed as a dual-Hanning window without adaptive optimization. However, the spectrum analysis accuracy of APFFT will significantly decrease under strong noise or interharmonic interference. SDS can take advantage of the inherent sparse characteristics of harmonic signals to effectively separate the principal components and noise and improve the robustness of parameter estimation. Therefore, this study introduces SDS into APFFT to construct an optimization model with sparse constraints to achieve high-precision and high-resolution estimation of harmonic parameters in a noisy environment.

SDS constructs an overcomplete Fourier dictionary and transforms the signal decomposition into a sparse optimization problem under L1-norm constraints. This mechanism allows the dominant harmonic components of the signal to be accurately represented by a small number of non-zero coefficients, while noise and side lobes associated with spectral leakage are effectively suppressed due to their inability to form sparse matches with the dictionary atoms, thereby significantly improving spectral purity [19]. For a given signal $\mathbf{y}$, the goal is to find the sparsest coefficient vector $\mathbf{a}$ in the overcomplete dictionary $\mathbf{D}$ such that $\mathbf{y} \approx \mathbf{D}\mathbf{a}$. This can be

Figure 3
Schematic diagram of the algorithmic framework of APFFT.

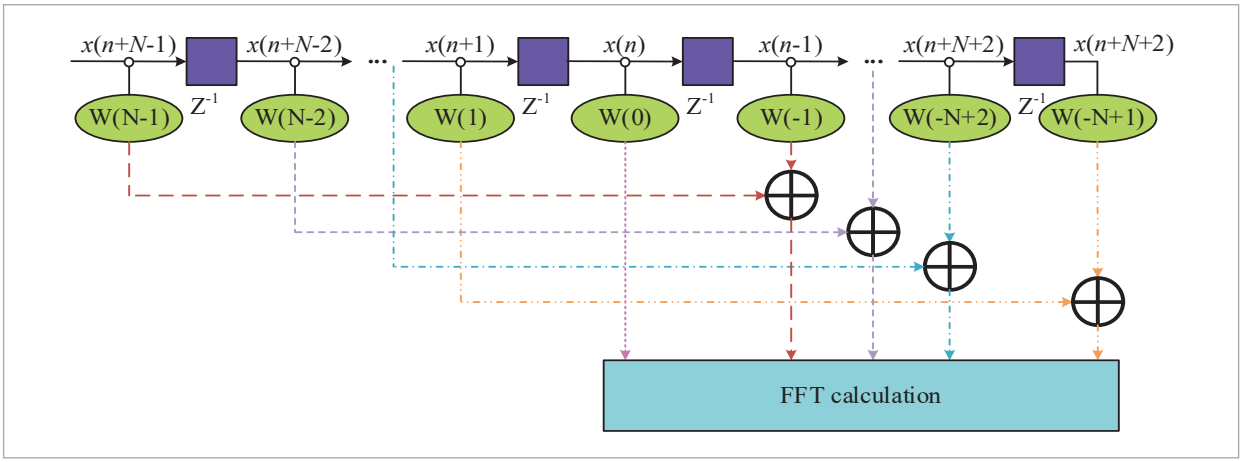
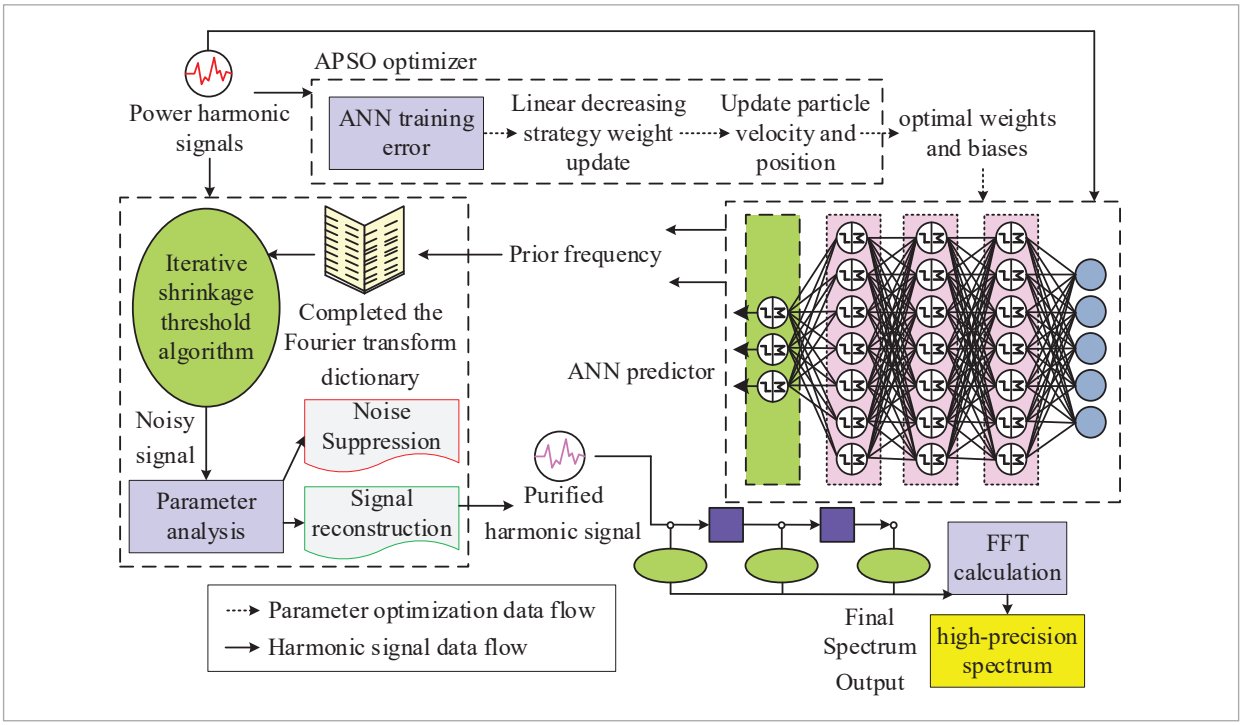


Figure 4
Schematic diagram of the structure of the A-AHDM harmonic detection model.



achieved by solving an L1-norm regularized least squares problem, thereby accurately reconstructing the main components of the signal and suppressing noise. First, an overcomplete Fourier dictionary $\mathbf{D}\in C^{N\times K}(K\gg N)$ is constructed based on the harmonic analysis range. Among them, the $\mathbf{d}_k$ form of each column of atoms is shown in Equation (9).

$$\mathbf{d}_k=\left[1,e^{j\omega_k},...,e^{j(N-1)\omega_k}\right]^T. \tag{9}$$

In Equation (9), j is an imaginary unit. ω_k represents the angular frequency of the k-th frequency component. The dimension of $\mathbf{D}$ is much larger than the

input signal length N, ensuring that it has sufficient redundancy to capture all potential frequency components of the signal [3]. For the input signal N, find the sparsest coefficient vector $\mathbf{a}$ such that $\mathbf{y} \approx \mathbf{D}\mathbf{a}$. The research is realized by solving the following least squares optimization problem with L1 norm regularization, as shown in Equation (10).

$$\min_{\mathbf{a}} \frac{1}{2}\left\|\mathbf{y} - \mathbf{D}\mathbf{a}\right\|_2^2 + \lambda\left\|\mathbf{a}\right\|_1 . \quad (10)$$

In Equation (10), λ is the regularization parameter, which is used to balance the signal reconstruction error and the sparsity of the coefficient vector. $\|\cdot\|_2$ represents the L2 norm, which measures the reconstruction error. $\|\cdot\|_1$ represents the L1 norm, which is used to promote the sparsity of the solution. In this study, λ is selected through cross-validation via grid search within the range of 10^{-3} to 10^{-1}, with the optimal value determined based on the balance curve between reconstruction error and sparsity on the validation set. To solve this problem, the iterative shrinkage-threshold algorithm is used to solve this problem. After solving, the position of the non-zero coefficient a_k corresponds to the harmonic frequency, and its value contains amplitude and phase information, thereby achieving high-precision parameter estimation [15]. SDS has the following parameters: frequency range from 45–55 Hz for the fundamental and its multiples for harmonics, atom spacing of 0.2 Hz, dictionary atoms normalised by L2 norm, regularisation parameter λ selected from {0.001, 0.005, 0.01, 0.05, 0.1}, ISTA step size set as the reciprocal of the maximum eigenvalue of the dictionary matrix, maximum iterations of 500, convergence tolerance of 0.0001, and non-zero coefficient threshold set to 1% of the maximum absolute coefficient value.

Therefore, it uses SDS as the filter of APFFT and establishes a high-precision harmonic parameter estimation module based on SDS-APFFT. This module first uses sparse decomposition to accurately separate the dominant harmonic components from the noisy signal, and then feeds the purified signal into the APFFT core for calculation, thereby obtaining unbiased, high-precision harmonic amplitude, frequency and phase estimation results even in a strong noise background. During this process, after sparse reconstruction by SDS, the dominant harmonic components are effectively extracted, while noise and side lobes associated with spectral leakage are suppressed. Since the phase invariance of APFFT is established on the basis of all-phase preprocessing and dual-window convolution, its underlying assumption has no direct correlation with the sparsity of the input signal; instead, the improvement in spectral purity brings the phase measurement closer to a theoretically unbiased estimate. From a quantitative perspective, the influence of residual noise and interharmonic components on the phase accuracy of APFFT mainly stems from their side lobe leakage interfering with the main lobe phase response, with the phase error being proportional to the amplitude of the residual components. Moreover, the effectiveness of SDS depends on the sparse representation capability of harmonic components; when the (signal-to-noise ratio, SNR) falls below 5 dB, the noise amplitude may exceed that of weak harmonic components, leading to incorrect atom selection and a significant degradation in filtering performance.

In summary, this study combines the preliminary harmonic feature extraction module and the high-precision harmonic parameter estimation module in series to establish an A-AHDM harmonic detection model. Its structure is shown in Figure 4.

In Figure 4, the final model forms a two-stage processing architecture. The front-end ANN-APSO module rapidly scans the original signal and performs robust preliminary extraction of harmonic features. Its output – preliminary estimates including the amplitude and frequency position of each harmonic – is encoded to generate a frequency band mask for the back-end SDS-APFFT module. By assigning high priority to the corresponding dictionary atoms in the sparse decomposition process, this mask guides the subsequent analysis to focus only on the key frequency bands identified by the front end for atomic selection and precise parameter estimation.

3. Results and Analysis

To verify the effectiveness of the proposed the ANN-APFFT-based harmonic detection model (A-AHDM) in power harmonic detection, simulation data experiments and real power grid scenario verification are implemented. The former uses

Gaussian and non-Gaussian mixed noise injection and interharmonic coupling interference simulation to quantitatively evaluate the harmonic parameter estimation accuracy and noise suppression capability. The latter is based on power signal data with complex background interference collected from actual industrial sites to verify the model's detection robustness and engineering applicability under strong noise and dynamic working conditions.

3.1. Simulation Data Experiment

In the simulation test, the algorithm requirements for harmonic detection in the power system are studied, and a corresponding experimental environment is built, which is divided into two parts: a hardware platform and a software platform. The specific configuration is shown in Table 2.

The training set and test set (divided 8:2 by time series) based on data from the Texas power grid in the United States and builds a hybrid power topology including industrial loads, commercial loads and residential loads. It continuously collects multi-source data streams from high-precision power quality analyzers (256 points/cycle), smart meters (1-minute intervals) and SCADA systems (second-level time scale), covering typical disturbance event markers such as motor start and stop, inverter switching and new energy fluctuations. Among them, the non-Gaussian mixed noise is synthesized by mixing Gaussian white noise and impulse noise in a 7:3 ratio, with the impulse noise generated using a Bernoulli-Gaussian model and an occurrence probability set to 0.05. The harmonic amplitudes are uniformly distributed within 0.5% to 20% of the fundamental amplitude, the phases are randomly selected within the range of $-\pi$ to π, and the interharmonic amplitudes are set to 30% to 60% of the amplitudes of their adjacent harmonics.

Moreover, the study selects the methods in the literature [5, 10, 26, 23] to compare with A-AHDM, which are based on TIEEMD, WFN-STS, RSDDL, and CNN and LSTM integrated harmonic detection method (CNLS) respectively. To ensure fairness in the comparison, the hyperparameters of all compared methods are tuned via grid search following the ranges suggested in their respective literature, and all methods are tested under the same training and test set split.

The study measures the phase measurement accuracy and frequency tracking stability of the model by comparing harmonic phase absolute error (HPAE) and frequency estimation root mean square error (FERMSE), HPAE is the absolute error between the estimated phase and the true phase (°); FERMSE is the root mean square error of frequency estimation, i.e., sqrt(mean((estimated frequency – true frequency)^2)) (mHz), as shown in Figure 5.

Table 2

Schematic diagram of the experimental platform configuration.

Category	Component	Specification/Version
Hardware	CPU	Intel Core i9-14900K
	RAM	64GB DDR5 5600MHz
	GPU	NVIDIA RTX 4090 (24GB GDDR6X)
	Storage	2TB NVMe SSD (PCIe 5.0)
	Data acquisition	NI PXIe-4499 24-bit High-Speed DAQ Module
Software	OS	Windows 11 Professional
	Deep learning framework	PyTorch 2.1 + CUDA 12.1
	Numerical computing	MATLAB R2023a
	Signal processing library	SciPy 1.11.4 / NumPy 1.26.4
	Programming language	Python 3.10.14
	Virtual environment	Anaconda 23.11.0

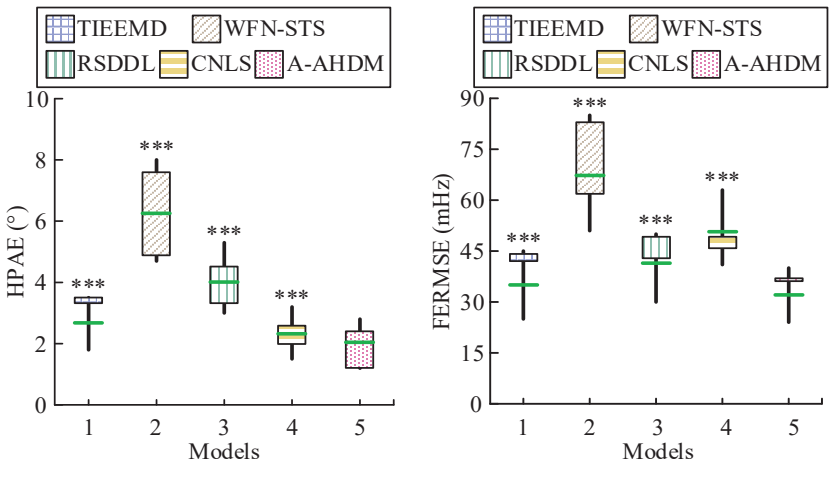
In Figure 5(a), the average HPAE value of A-AHDM is 2.05°, which is significantly better than the comparison method (p<0.001). It effectively guarantees the phase measurement accuracy through APFFT phase invariance and SDS spectrum purification. While TIEEMD has limited accuracy due to modal aliasing (2.69°) caused by endpoint effects, the WFN-STS control strategy performs the worst with insufficient phase sensitivity (6.25°). RSDDL is insufficiently stable due to the phase annotation error of the training data (4.02°). Although CNLS takes advantage of timing modeling (2.33°), it has not broken through the limitations of traditional phase detection. In Figure 5(b), the average FERMSE of A-AHDM is optimal at 32.03mHz (p<0.001), which achieves accurate frequency tracking through all-phase spectrum analysis and fixed dual-Hanning window filtering. The spectrum leakage effect of TIEEMD (34.97mHz) restricts the frequency resolution, and the control system response delay of WFN-STS (67.23mHz) leads to the deterioration of dynamic tracking performance. RSDDL has insufficient adaptability to frequency mutations (41.39mHz), and CNLS has significant frequency estimation errors due to long sequence dependency modeling bias (50.61mHz).

The study verifies the effectiveness and rationality of the basic modules selected for the study by ablating the basic modules and replacing them with support vector machine (SVM), differential evolution (DE), short-time Fourier transform (STFT) and orthogonal matching pursuit (OMP). The selected metrics are FERMSE, convergence time (CT), and floating point operations (FLOPs). CT is the convergence time from algorithm start until the detection result stabilises within a preset error band (ms); FLOPs is the total number of single-precision floating-point operations required for one complete detection run (M, millions), as shown in Table 3.

In Table 3, the complete A-AHDM model reaches the optimal level in all indicators, verifying the effectiveness of its module design. In the ablation experiment, removing the APSO optimizer (A1) caused HARE to increase to 2.31% (p<0.01). This shows that parameter pre-optimization plays a key role in improving detection accuracy. Meanwhile, the performance further deteriorated when APSO and SDS (A3) are removed, with HARE reaching 2.87% (p<0.001), proving the necessity of dual-module collaborative optimization. Although removing ANN (A4) reduces the calculation amount, HARE deteriorates to 3.26% (p<0.001), highlighting the core value of intelligent feature extraction. In the module replacement experiment, SVM replaced ANN to increase HARE to 2.94% (p<0.001), verifying the advantages of ANN in nonlinear mapping. Replacing APSO with DE causes CT to increase to 68.3ms (p<0.01), reflecting the superiority of APSO in convergence speed. Replacing

Figure 5

Comparison of HPAE and FERMSE for different algorithms.



(a) Comparison of HPAE (b) Comparison of FERMSE

Table 3
Validation of the effectiveness of basic modules.

Model types		ANN	APSO	APFFT	SDS	FERMSE (mHz)	CT (ms)	FLOPs (M)
Full	A-AHDM	√	√	√	√	32.03	40.2	1.41
Ablation	A1	√	×	√	√	38.72	47.6	1.43
	A2	√	√	√	×	36.45	42.3	1.39
	A3	√	×	√	×	45.63	49.8	1.42
	A4	×	×	√	√	51.37	38.9	1.12
Replacement	SVM	-	√	√	√	43.28	52.7	1.85
	DE	√	-	√	√	39.64	68.3	2.17
	STFT	√	√	-	√	47.51	35.4	2.86
	OMP	√	√	√	-	41.72	44.1	2.34

APFFT with STFT increases FERMSE to 47.51mHz (p<0.001), proving the irreplaceability of full-phase transformation in frequency accuracy. Although OMP replaces SDS, it maintains a lower HARE (2.19%), but FLOPs increase to 2.34M (p<0.05), indicating that SDS achieves the best balance between accuracy and efficiency.

3.2. Real Power Grid Scenario Verification

Actual measurement verification can reflect the complexity of electromagnetic disturbances in the real power grid environment to verify the reliability of the detection algorithm in industrial sites, especially its adaptability to transient harmonics and background noise. Therefore, the study selects CNLS and TIEEMD, which have excellent performance in simulation verification, as comparison methods to conduct multi-scenario actual measurement verification. To verify the robustness and theoretical accuracy limit of the model in a noisy environment, the study compared the noise robustness gain (NRG) and inherent estimation error (IEE) of different models after introducing Gaussian noise (SNR=5dB/15dB/30dB). NRG is the difference between output SNR and input SNR (dB); IEE is the relative error between the estimated value and the true value under ideal noise-free conditions (%), as shown in Figure 6.

In Figure 6(a), in a 5dB to 30dB noise environment, the NRG of TIEEMD improves from 5.8dB to 10.5dB, and the IEE improves from 1.8% to 0.8%. The data shows that this method is sensitive to changes in noise levels, and its performance degrades significantly under low signal-to-noise ratio conditions. Its signal decomposition mechanism is seriously affected by modal aliasing in a strong noise environment (5dB), with limited NRG improvement and high IEE. As the noise level decreases, the decomposition accuracy gradually improves. However, the IEE still reaches 0.8% in a 30dB clean environment, showing that there is an inherent end-point effect error. In Figure 6(b), CNLS shows a stable performance improvement trend under three noise levels, with NRG increasing from 6.5dB to 11.2dB and IEE decreasing from 1.5% to 0.6%. Compared with TIEEMD, its deep learning architecture shows advantages in noise adaptability, especially the IEE is controlled at 1.0% at medium noise levels (15dB). However, in a 5dB strong noise environment, the neural network's erroneous learning of noise characteristics leads to a high IEE, while under 30dB conditions, the inherent fitting bias of the recurrent neural network limits its further improvement in accuracy. In Figure 6(c), A-AHDM maintains optimal performance under all noise levels, with NRG significantly improved from 9.2dB to 14.8dB and IEE significantly reduced from 1.0% to 0.2%. In a 5dB harsh environment, it effectively suppresses noise interference through the SDS-APFFT collaborative mechanism. Moreover, the study also compares the CPU utilization (CU) and memory usage (MU) of different models in actual deployment. CU is the average

CPU usage during algorithm operation (%); MU is the peak memory usage during algorithm operation (MB), as shown in Figure 7.

In Figure 7(a), the average CPU utilization of A-AHDM is 31.42%, which is significantly lower than that of CNLS (35.65%, $p<0.001$). Although TIEEMD has the lowest CPU usage (21.32%), A-AHDM achieves a favorable balance between computational cost and detection accuracy, as evidenced by its superior performance in harmonic estimation. In Figure 7(b), A-AHDM achieves a competitive MU average of 151.26MB. Although TIEEMD uses lower memory (137.87MB) and CPU (21.32% vs. 31.42%), A-AHDM offers a better accuracy–resource

Figure 6

Comparison of NRG and IEE for different algorithms under 5dB-30dB Gaussian noise.

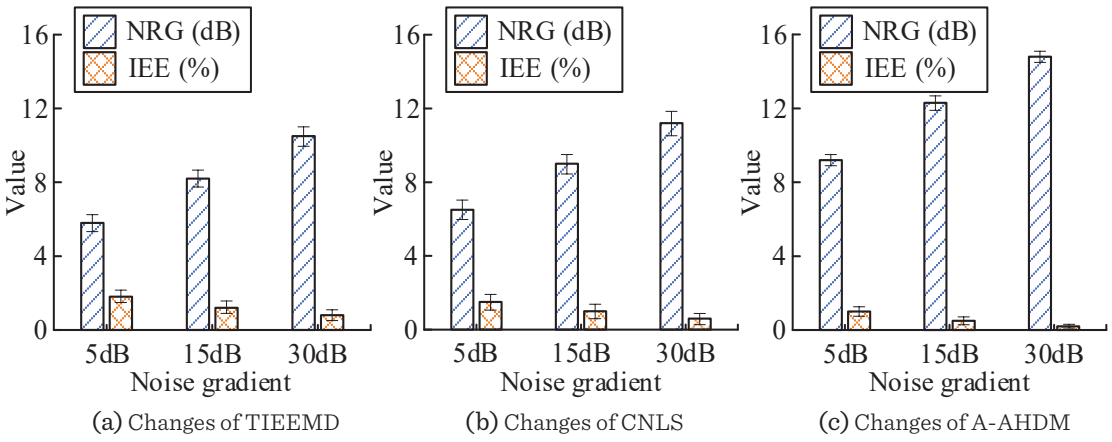


Figure 7

Validation of practical deployment feasibility.

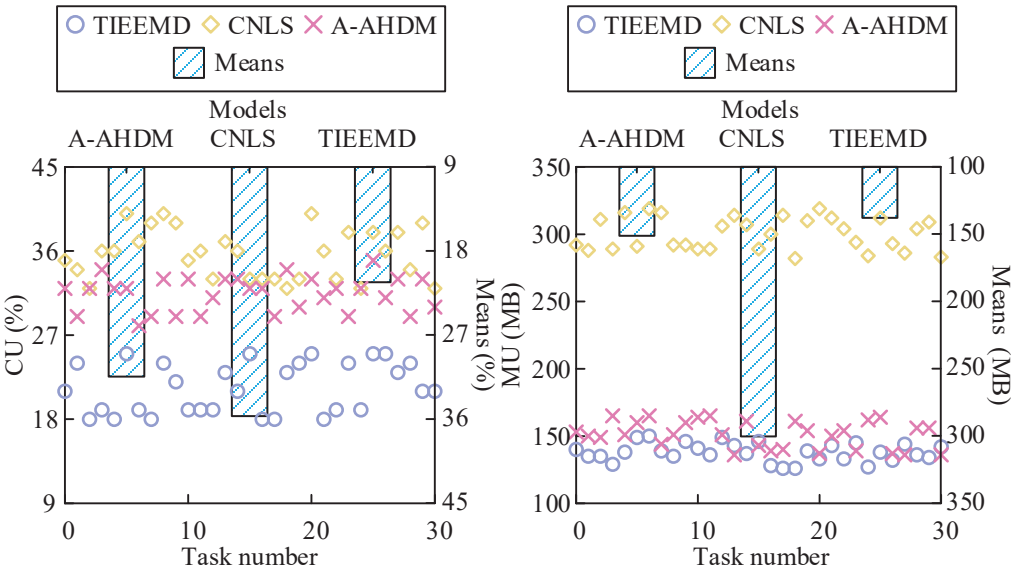


Table 4
Validation of dynamic response speed and operating condition adaptability.

Transient event	Models	TPCT (ms)						
		0	1	2	3	4	5	6
Motor starting	TIEEMD	117	140	111	135	113	128	140
	CNLS	120	111	120	101	118	119	104
	A-AHDM	97	103	98	95	102	93	88
Capacitor bank switching	TIEEMD	49	46	52	57	47	57	48
	CNLS	54	46	49	48	49	40	51
	A-AHDM	32	42	33	30	42	31	39
Short-circuit fault clearing	TIEEMD	196	171	196	197	178	151	182
	CNLS	168	132	132	132	160	132	131
	A-AHDM	141	137	132	130	118	114	130

trade_off by maintaining high detection precision with moderately increased computational cost, as supported by its significantly lower HARE (1.65% vs. 3.26%) and FERMSE (32.03mHz vs. 51.37mHz) compared to TIEEMD. By comparing the transient process convergence time (TPCT) of different methods under different events, the dynamic response speed and working condition adaptability of the model are measured. TPCT is the time from the occurrence of a transient event until the detection result first enters and remains within the steady-state error band, as shown in Table 4.

In Table 4, in the motor starting scenario, the average transient CT value of A-AHDM is 96.6ms, which is significantly better than TIEEMD (126.9ms, $p<0.01$) and CNLS (113.3ms, $p<0.05$). Through the fast feature extraction capability of the APSO-ANN module, it takes the lead in completing stable tracking during slowly changing transient processes. In the capacitor bank switching scenario, A-AHDM maintains the lead with a convergence speed of 35.6ms (TIEEMD: 50.9ms, $p<0.001$; CNLS: 48.1ms, $p<0.01$). The SDS-APFFT combination has excellent suppression capabilities for high-frequency oscillation components and significantly accelerates the convergence of the transient process. In the short-circuit fault clearing scenario, A-AHDM shows the strongest dynamic adaptability (mean value 128.9ms), which is 28.9% and 8.6% higher than TIEEMD (181.3ms, $p<0.001$) and CNLS (141.0ms, $p<0.05$) respectively. Its collaborative mechanism of intelligent front-end and precision back-end can still maintain fast response characteristics under large disturbance conditions. The improvement in convergence speed of A-AHDM means that during transient processes such as motor starting, the harmonic parameter detection results can stabilize to the true value range more quickly, thereby providing relay protection devices with more timely and accurate harmonic state information, shortening the start-up delay of protection criteria, and securing an earlier intervention window for oscillation damping control. To verify the detection robustness of A-AHDM under extreme power system conditions and its deployment feasibility on resource-constrained platforms, three typical extreme operating conditions – harmonic oscillation, sub-synchronous oscillation aliasing, and frequency rapid slip – are selected for comparative testing on an ARM Cortex-A76 embedded platform (4 cores, 2.1 GHz) and an RTX 4090 high-end platform. The selected metrics are the Harmonic Amplitude Relative Error (HARE), FERMSE, and TPCT. HARE is the relative error between the estimated amplitude and the true amplitude, i.e., |estimated amplitude – true amplitude| / true amplitude × 100% (%). The results are presented in Table 5.

Table 5
Validation of detection performance under extreme operating conditions.

Extreme condition	Platform	HARE (%)	FERMSE (mHz)	TPCT (ms)
Harmonic oscillation	RTX 4090	2.12	45.36	82.4
	ARM	2.34	48.71	156.3
Sub-synchronous oscillation aliasing	RTX 4090	2.56	52.18	94.7
	ARM	2.81	57.63	178.2
Frequency rapid slip	RTX 4090	1.98	41.25	78.6
	ARM	2.19	44.92	149.5

In Table 5, on the RTX 4090 platform, A-AHDM achieves HARE values of 2.12%, 2.56%, and 1.98%, FERMSE values of 45.36 mHz, 52.18 mHz, and 41.25 mHz, and TPCT values of 82.4 ms, 94.7 ms, and 78.6 ms, respectively, demonstrating good detection accuracy and convergence speed. Among these, the sub-synchronous oscillation aliasing condition, characterized by dense frequency components and complex modal coupling, yields slightly inferior performance compared to the other two conditions, but remains within an acceptable range, confirming the model's robustness against complex dynamic disturbances. The acceptable range is defined as HARE ≤3%, FERMSE ≤60 mHz (per IEC 61000-4-30 and IEEE C37.118.1), and HPAE ≤5°. On the ARM embedded platform, the model maintains detection effectiveness, with HARE and FERMSE increasing only slightly by 0.22% to 0.45% compared to the high-end platform, indicating that the core mechanisms of sparse decomposition and all-phase analysis remain stable under resource-constrained conditions. However, TPCT increases significantly due to computational resource limitations, reaching 156.3 ms, 178.2 ms, and 149.5 ms across the three conditions – approximately 1.9 times that of the high-end platform – suggesting that the real-time performance of the algorithm on resource-constrained devices still requires further optimization.

4. Discussion and Conclusions

In view of the core problems existing in power system harmonic detection, such as inaccurate feature extraction, sensitivity to noise interference, and slow dynamic response, this study proposed an ANN-APFFT-based harmonic detection model (A-AHDM). This study used the APSO-ANN module to achieve robust preliminary extraction of harmonic features, and combined it with the SDS-APFFT module to complete precise parameter estimation, building a series architecture of "rapid feature extraction-precise parameter estimation". It effectively solved the contradiction between detection accuracy and anti-interference ability of traditional methods. Experimental results showed that A-AHDM was significantly better than the comparison method in key indicators such as phase measurement accuracy (HPAE: 2.05°) and frequency tracking stability (FERMSE: 32.03mHz) (p<0.001). Meanwhile, this method remained leading in terms of dynamic response speed (TPCT: 35.6–128.9ms). This verified its comprehensive advantages in detection accuracy, robustness and engineering applicability. The innovation of A-AHDM was that the APSO-ANN module improved the quality of the initial parameters of the neural network through APSO. It overcome the shortcomings of traditional ANN that easily fall into local optimality and ensures the stability of feature extraction. The SDS-APFFT module significantly enhanced the anti-interference ability of full-phase spectrum analysis in noisy environments through SDS pre-filtering. The series architecture combines the complementary advantages of intelligent learning and mathematical analysis, effectively solving the problem of insufficient detection performance of a single method in complex harmonic scenarios. Despite the computational overhead of APSO optimisation and SDS

iteration, experimental results show that the algorithm achieves a convergence time below 50 ms on high-end platforms (meeting the protection_level requirement of ≤50 ms) and within 200 ms on ARM platforms (meeting the monitoring_level requirement of ≤200 ms, based on IEC 61000_4_30). This latency satisfies the real_time requirements of most power quality monitoring and protection applications, and is therefore acceptable.

However, the research still has certain limitations: The APSO optimization effect depends on the initial hyperparameter settings, which may affect the convergence efficiency in extreme noise environments. The "over-complete" dictionary construction of SDS requires prior knowledge support, and its adaptability to unknown harmonic types needs to be strengthened. The real-time performance of the full algorithm on resource-constrained devices still needs to be further optimized. The current model has been validated within the 2nd to 25th harmonic range, but its adaptability to higher-order harmonics, supra-harmonics, or signals with fast time-varying frequencies is constrained by the network input dimension and the frequency resolution of the overcomplete dictionary, which limit the spectral coverage and time-frequency tracking capability. The preliminary estimation error (e.g., frequency deviation) from the front-end ANN-APSO module is passed to the back-end SDS-APFFT module, affecting the frequency parameter settings of its dictionary atoms. The degree of influence of this error on the final detection accuracy is negatively correlated with the dictionary resolution, and can be neglected when the frequency deviation is less than half the atom interval. To address the above issues, future work will design an adaptive hyperparameter optimization framework and combine meta-learning technology to improve model self-adjustment capabilities. A dynamic dictionary update mechanism needs to be developed to enhance the ability to identify new harmonics through online learning. It is necessary to study model lightweight solutions and implement edge device deployment based on neural network pruning and quantification technology. An extensible network structure will be introduced to adaptively adjust the network dimension through an attention mechanism, and the frequency atomic library will be dynamically expanded through online dictionary learning. An iterative calibration mechanism based on residual feedback will be introduced, where the deviation between the high-precision estimation results from the back-end module and the preliminary estimation results from the front-end module is used to construct an error correction signal, and the front-end output is progressively corrected through closed-loop iterations to reduce the sensitivity to error propagation.

References

1. Agrawal, S., Palwalia, D. K., Kumar, M. Performance Analysis of ANN-Based Three-Phase Four-Wire Shunt Active Power Filter for Harmonic Mitigation Under Distorted Supply Voltage Conditions. IETE Journal of Research, 2022, 68(1), 566-574. https://doi.org/10.1080/03772063.2019.1617198
2. Caicedo, J. E., Agudelo-Martínez, D., Rivas-Trujillo, E., Meyer, J. A Systematic Review of Real-Time Detection and Classification of Power Quality Disturbances. Protection and Control of Modern Power Systems, 2023, 8(1), 1-37. https://doi.org/10.1186/s41601-023-00277-y
3. Ding, T., Chen, H., Chen, L., Shi, J., Zhou, Y. Improved Sparse Component Analysis for Multi-Point Harmonic Contribution Evaluation Under Incomplete Measurements. IEEE Transactions on Power Delivery, 2022, 37(5), 4019-4031. https://doi.org/10.1109/TPWRD.2022.3142968
4. Duc, M. L., Tan, D. P. Single Phase Harmonic Mitigation Using Particle Swarm Optimization in Shunt Adaptive Power Filter. International Journal of Engineering Technology and Management Sciences, 2023, 7(1), 239-247. https://doi.org/10.46647/ijetms.2023.v07i05.028
5. Fei, J., Zhang, L., Zhuo, J., Fang, Y. Wavelet Fuzzy Neural Supertwisting Sliding Mode Control of an Active Power Filter. IEEE Transactions on Fuzzy Systems, 2023, 31(11), 4051-4063. https://doi.org/10.1109/TFUZZ.2023.3272028
6. Gao, M., Yang, X. APSO-SL: An Adaptive Particle Swarm Optimization with State-Based Learning

Strategy. Processes, 2024, 12(2), 400. https://doi.org/10.3390/pr12020400

7. Hosseinpour, A., Sadeq, M. O. Harmonic Reduction of Current by Using Phase Shifting and Shunt-Active Filter Trained by Fuzzy Particle Swarm Optimization. International Journal of Fuzzy Systems, 2022, 24(6), 2729-2739. https://doi.org/10.1007/s40815-022-01275-2
8. Ibanez-Hidalgo, I., Sanchez-Ruiz, A., Perez-Basante, A., Zubizarreta, A., Ceballos, S., Gil-Lopez, S., Aguilera, R. P. Real-Time Selective Harmonic Control-PWM Based on Artificial Neural Networks. IEEE Transactions on Power Electronics, 2024, 39(1), 768-783. https://doi.org/10.1109/TPEL.2023.3322500
9. Jamlaay, M. Three Phase Series Active Power Filter Based Adaptive Linear Neuron (ADALINE) to Overcome Voltage Harmonics in Power Systems. International Journal of Science and Technology Management, 2024, 5(1), 242-248. https://doi.org/10.46729/ijstm.v5i1.1054
10. Kuyumani, E. M., Hasan, A. N., Shongwe, T. A Hybrid Model Based on CNN-LSTM to Detect and Forecast Harmonics: A Case Study of an Eskom Substation in South Africa. Electric Power Components and Systems, 2023, 51(8), 746-760. https://doi.org/10.1080/15325008.2023.2181883
11. Liu, H., Yao, W., Bi, T., Li, J. Dynamic Wideband Synchrophasor Measurement Method with High-Frequency Resolution. IEEE Transactions on Instrumentation and Measurement, 2025, 74(1), 1-11. https://doi.org/10.1109/TIM.2025.3547540
12. Liu, Y., Xu, X., Yang, Z. Application of Harmonic and Interharmonic Detection in Ship Power Network Based on HT-SVD Transform. International Core Journal of Engineering, 2022, 8(4), 416-433. DOI: 10.6919/ICJE.202204_8(4).0053.
13. Mbarki, B., Chrouta, J., Khaterchi, H., Farhani, F., Zaafouri, A. Efficiency Optimization of a Photovoltaic System Using Adaptive Particle Swarm Optimization and Neural Network Based on Robust Terminal Sliding Mode Control for Maximum Power Point Tracking. International Journal of Dynamics and Control, 2025, 13(6), 208. https://doi.org/10.1007/s40435-025-01720-8
14. Rafique, W., Khan, A., Almogren, A., Arshad, J., Yousaf, A., Jaffery, M. H., Shafiq, M. Adaptive Fuzzy Logic Controller for Harmonics Mitigation Using Particle Swarm Optimization. Computers, Materials & Continua, 2022, 71(3), 4275-4293. https://doi.org/10.32604/cmc.2022.023588
15. Richardson, N., Schaeffer, H., Tran, G. SRMD: Sparse Random Mode Decomposition. Communications on Applied Mathematics and Computation, 2024, 6(2), 879-906. https://doi.org/10.1007/s42967-023-00273-x
16. Rodrigues, N. M., Janeiro, F. M., Ramos, P. M. Deep Learning for Power Quality Event Detection and Classification Based on Measured Grid Data. IEEE Transactions on Instrumentation and Measurement, 2023, 72(1), 1-11. https://doi.org/10.1109/TIM.2023.3293555
17. Sangeeth, B. K., Vinod, V. High Impedance Fault Detection Using Multi-Domain Feature with Artificial Neural Network. Electric Power Components and Systems, 2023, 51(4), 366-379. https://doi.org/10.1080/15325008.2023.2172091
18. Sapkota, D. B., Neupane, P., Pokharel, K., Khan, S. An Artificial Neural Network-Based Approach for Harmonic Component Prediction in a Distribution Line. Energy Reports, 2024, 12(1), 3861-3873. https://doi.org/10.1016/j.egyr.2024.09.060
19. Sharma, M., Rajpurohit, B. S., Agnihotri, S., Singh, S. N. Data Analytics Based Power Quality Investigations in Emerging Electric Power System Using Sparse Decomposition. IEEE Transactions on Power Delivery, 2022, 37(6), 4838-4847. https://doi.org/10.1109/TPWRD.2022.3160613
20. Song, G., Cao, B., Chang, L. A Passive Islanding Detection Method for Distribution Power Systems with Multiple Inverters. IEEE Journal of Emerging and Selected Topics in Power Electronics, 2022, 10(5), 5727-5737. https://doi.org/10.1109/JESTPE.2022.3165631
21. Sun, B., Wu, X., Chen, X., Zou, Z., Li, Q., Ren, B. Parameter Estimation of Sub-/Super-Synchronous Oscillation Based on Interpolated All-Phase Fast Fourier Transform with Optimized Window Function. Journal of Modern Power Systems and Clean Energy, 2024, 12(4), 1031-1041. https://doi.org/10.35833/MPCE.2023.000179
22. Toubal Maamar, A. E., Helaimi, M. H., Taleb, R., Kermadi, M., Mekhilef, S. A Neural Network-Based Selective Harmonic Elimination Scheme for Five-Level Invert-

er. International Journal of Circuit Theory and Applications, 2022, 50(1), 298-316. https://doi.org/10.1002/cta.3130

23. Wang, R., Huang, W., Hu, B., Du, Q., Guo, X. Harmonic Detection for Active Power Filter Based on Two-Step Improved EEMD. IEEE Transactions on Instrumentation and Measurement, 2022, 71(1), 1-10. https://doi.org/10.1109/TIM.2022.3146913
24. Wang, Y., Yu, M., Ma, X., Xiao, X., Wang, C., Liu, C. A General Harmonic Probability Model Based on Load Operating States Identification. IEEE Transactions on Power Delivery, 2023, 38(4), 2247-2260. https://doi.org/10.1109/TPWRD.2022.3213646
25. Yuan, J., Hu, Y., Liang, Y., Jiao, Z. Faulty Feeder Detection for Single Line-to-Ground Fault in Distribution Networks with DGs Based on Correlation Analysis and Harmonics Energy. IEEE Transactions on Power Delivery, 2023, 38(2), 1020-1029. https://doi.org/10.1109/TPWRD.2022.3203992
26. Zhang, Z., Yi, H., Zhuo, F., Li, Y., Jiang, X. Harmonic Oscillation Analysis and Stabilization Method Comparison of Shunt Active Power Filter in Full Compensation Mode. IET Power Electronics, 2024, 17(9), 1145-1158. https://doi.org/10.1049/pel2.12612

This article is an Open Access article distributed under the terms and conditions of the Creative Commons Attribution 4.0 (CC BY 4.0) License (http://creativecommons.org/licenses/by/4.0/).